Nucleation of Dislocations in 3.9 nm Nanocrystals at High Pressure

Authors: Abhinav Parakh[1], Sangryun Lee[2], K. Anika Harkins[3], Mehrdad T. Kiani[1], David Doan[4], Martin Kunz[5], Andrew Doran[5], Lindsey A. Hanson[3], Seunghwa Ryu[2] and X. Wendy Gu[4]*

Affiliations:

[1]Materials Science and Engineering, Stanford University, Stanford, CA 94305, USA.

[2]Mechanical Engineering, KAIST, Yuseong-gu, Daejeon 34141, Republic of Korea.

[3] Chemistry, Trinity College, Hartford, CT 06106, USA.

[4]Mechanical Engineering, Stanford University, Stanford, CA 94305, USA.

[5]Advanced Light Source, Lawrence Berkeley National Lab, Berkeley 94720, USA.

*Corresponding author:

X. Wendy Gu

452 Escondido Mall, Room 227, Stanford University, Stanford, CA 94305

650-497-3189

xwgu@stanford.edu

Abstract:

As circuitry approaches single nanometer length scales, it has become important to predict the stability of single nanometer-sized metals. The behavior of metals at larger scales can be predicted based on the behavior of dislocations, but it is unclear if dislocations can form and be sustained at single nanometer dimensions. Here, we report the formation of dislocations within individual 3.9 nm Au nanocrystals under nonhydrostatic pressure in a diamond anvil cell. We used a combination

of x-ray diffraction, optical absorbance spectroscopy, and molecular dynamics simulation to characterize the defects that are formed, which were found to be surface-nucleated partial dislocations. These results indicate that dislocations are still active at single nanometer length scales and can lead to permanent plasticity.

Main text:

Permanent plastic deformation occurs in bulk crystalline metals that are subjected to large strains at room temperature. This irreversible deformation can be due to the short-range interactions between dislocations, or the formation of dislocation arrays at grain or twin boundaries. Recently, reversible deformation from large strains has been observed in sub-10 nm Ag nanocrystals [1] and 3.9 nm Au nanocrystals, [2] in which the nanocrystal rapidly recovers from a flattened state after load is removed, and reverts to its original faceted shape. The mechanisms behind this behavior remain unclear, as there is evidence for both diffusion and dislocation mediated plasticity. Rapid diffusion of atoms at free surfaces and stress-induced diffusion at the nanocrystal-indenter and nanocrystal-substrate interfaces have been proposed as mechanisms, based on theoretical considerations and *in situ* transmission electron microscope (TEM) observations [1,3]. Others have instead observed surface-nucleated dislocations and deformation twinning in sub-10 nm nanowires, and stacking faults tetrahedra in sub-20 nm nanowires under tension in both experiments and molecular dynamics (MD) simulations [4–7]. Dislocations and diffusion may also act cooperatively. *In situ* TEM tension tests on ~20 nm and sub 5 nm Ag nanowires showed that surface diffusion is enhanced at surface steps created by the passage of dislocations [8,9]. Previous work from our group showed that pseudoelastic shape recovery (diffusion mediated

process) in 3.9 nm Au nanocrystals is accompanied by the formation of irreversible defects, but the nature of the defects could not be determined [2].

These observations prompt the questions: Is there a limit to plasticity at small length scales? What is the smallest crystal in which dislocations can form and lead to irreversible deformation? This is critical to the processing and mechanical behavior of nanostructured materials such as nanocrystalline, nanotwinned and nanoporous metals, and the design of stable nano-devices with single nanometer metallic features [10]. To answer these questions, deformation mechanisms in very small nanocrystals must be experimentally determined, but this remains challenging. *In situ* TEM mechanical testing is the leading method to investigate deformation mechanisms at this length scale, but results may be influenced by heating from the electron beam. In addition, fast dislocations and dislocations that are invisible at specific imaging conditions cannot be observed. X-ray diffraction (XRD) is another method to measure elastic strain and defect formation in metals under mechanical stress. The width and relative intensities of XRD peaks have previously been used to detect dislocation activity in nanocrystalline Ni under uniaxial tension [11] and compression in a diamond anvil cell (DAC) [12]. These studies involve the response at grain boundaries as well as within the grains, so they cannot be directly applied to understand plasticity in individual nanocrystals. To do this, the structural response of isolated nanocrystals must be obtained. This presents a challenge for *in situ* XRD because the diffracted intensities from a single nanocrystal are much too small for detection.

Here, we use XRD to detect structural changes in an ensemble of monodisperse 3.9 nm Au nanocrystals that are compressed under a non-hydrostatic pressure in a DAC. Surfaces of the nanocrystals are protected by organic ligands, which prevents contact between the nanocrystals. Structural changes from XRD are corroborated with optical spectroscopy measurements, and MD

simulations are used to determine the specific defects that correspond to the ensemble-averaged behavior from XRD. We show that irreversible deformation due to the formation of surface nucleated partial dislocations can occur in small metallic nanocrystals. This indicates that dislocation-mediated plasticity is still active at single nanometer length scales and must be considered in designing structures at this scale. Theoretical work on homogenous dislocation nucleation has been studied well for nanoindentation experiments on larger nanocrystals [new refs]. However, these results prompt for development of theoretical work on heterogenous dislocation nucleation from nanocrystal surface in compression in DAC.

Au nanocrystals were synthesized using the organic phase reduction of chloroauric acid and capped with dodecanethiol ligands [13]. The nanocrystal size distribution was found to be 3.9±0.6 nm using TEM (see Fig. 1A and see the Supplementary Material [14]). High-resolution TEM images showed that most of the identified nanocrystals were either icosahedral or decahedral in shape (Fig. 1B-C). Icosahedral nanocrystals have 20 twin boundaries, and decahedral nanocrystals have 5 twin boundaries. Ambient pressure XRD showed an FCC crystal structure, and significantly broader peaks than bulk Au due to the limited coherent scattering volume within the nanocrystals (see the Supplementary Material [14]). The (111), (220), (311) and (222) XRD peaks were shifted to higher 2θ angles by ~0.1^{o} compared to that of the bulk, which corresponds to a ~1.8% volumetric compressive strain. The position of the (200) peak was shifted to lower 2θ angles by 0.15^{o}. Broad shoulders were observed on the (200) and (220) peaks. These features are indicative of the high twin density in icosahedral and decahedral nanocrystals [22]. In addition, the (111) peak showed asymmetric broadening due to tensile and compressive stresses at the surfaces and the interior of the nanocrystals due to surface stresses [30]. The Au nanocrystals consist of ~20% surface atoms with most of the surface covered with (111) planes. As a result, the

(111) peak shows the most asymmetrical broadening compared to the other peaks. The Debye scattering equation was used to fit the XRD pattern to determine the structure of the nanocrystals. In this method, the atomic positions for icosahedral and decahedral nanocrystals were generated for 1 to 6 nm diameter nanocrystals and used to simulate XRD patterns. A Rietveld-like refinement procedure was used to fit the experimental data [22,24]. The best fit was obtained by combining 60% icosahedral nanocrystals with a size distribution of 3.2±0.2 nm and 40% decahedral nanocrystals with a size distribution of 3.8±0.6 nm (see the Supplementary Material [14]). This result is in close agreement with the nanocrystal shape and size distribution observed in TEM.

High pressure XRD was obtained during DAC compression experiments at the Advanced Light Source at Lawrence Berkeley National Laboratory (Fig. 2A-B). A non-hydrostatic pressure was applied to the nanocrystals by loading the nanocrystals as a thick film at the bottom of the DAC sample chamber, and using toluene as a non-hydrostatic pressure medium [31]. XRD was collected while the nanocrystals were loaded up to 7.5 GPa and as pressure was released. The pressure was limited to 7.5 GPa to avoid sintering between the nanocrystals, which has been observed by our group and others at higher pressures [32–34]. The XRD peak position and width (full width at half max) were observed to change with increasing and decreasing pressure and quantified at each pressure (Fig. 2C-D). The relative intensity of the XRD peaks does not change under pressure, which indicates that the nanocrystals remain randomly oriented.

The change in peak position indicates the elastic strain in the nanocrystals. The shift in the peak position shows that the lattice spacing decreases by 0.042 Å over 7.5 GPa and recovers to ~0.2% of its original value upon unloading. The (200) peak position gives information about the extent of twinning in the sample (see Fig. S8 for the qualitative effect of twinning on the XRD peak). The complete recovery of the (200) peak position indicates that the initial multiply twinned

structure (icosahedral/decahedral) is preserved after the pressure cycle. Due to the non-hydrostatic pressure, the change in lattice spacing is different along the loading axis (axial) and orthogonal to the loading axis (radial). The geometry of the X-ray setup is such that the measured lattice spacings correspond to planes that are almost aligned with the loading axis. Therefore, the measured change in lattice spacing is lower than in the hydrostatic case (see the Supplementary Material [14]). The difference between radial and axial stress components (termed as t) can give us an estimate of maximum deviatoric and shear stresses in the system. This difference can be calculated by considering the elastic anisotropy of a polycrystalline, FCC metal. We used lattice strain theory to get a rough estimate of 't' [29,35] (see the Supplementary Material [14]). Using this we estimated the maximum shear stress of Au nanoparticles to be about 2.3 GPa (see the Supplementary Material [14]).

Fig. 2D shows the change in peak width for the (111), (200) and (220) peaks with a complete pressure cycle. The (200) peak width showed a significant increase of 16% and the (220) peak width showed an increase of 23% with increasing pressure and remained at higher values after unloading. This indicates that irreversible deformation is occurring in the nanocrystals and remains in the nanocrystals on the time scale of the experimental measurements. The XRD peak width can be affected by changes in crystallite size, shape and microstrain [36]. It is possible that crystalline domains within the nanocrystal become elongated under compression and split into smaller domains, but post-compression TEM images showed that the nanocrystal shape and size distribution is identical to that of the as-synthesized nanocrystals (see the Supplementary Material [14]). The (111) peak width is mostly affected by domain size changes and is least affected by the presence of defects like twinning and stacking faults in the nanocrystal (see the Supplementary Material [14]). The peak width for (111) peak remained at about 2% of its initial

value with pressure cycling. The insignificant change in the (111) peak width also indicates that domain size does not change under pressure [22,37]. From this analysis, we determine that the increased peak width after unloading is caused by the formation of crystalline defects such as dislocations rather than changes in the size and shape of crystalline domains. The observation that (200) and (220) peak were the most affected and the (111) peak is least affected indicates the presence of stacking faults, twinning and dislocations (see the Supplementary Material [14]).

These XRD results were corroborated by high-pressure optical absorbance spectroscopy. Au nanocrystals have a plasmonic resonance that is dependent upon nanocrystal size, shape and microstructure [38]. Previous optical modeling showed that the plasmon peak wavelength is indicative of nanocrystal shape, while an irreversible decrease in the plasmon peak intensity is indicative of the formation of crystalline defects [2]. The plasmon peak wavelength of the 3.9 nm Au nanocrystals increased by ~30 nm when pressure was increased to 7.5 GPa and recovered its initial value upon unloading (see the Supplementary Material [14]). These optical measurements showed that the nanocrystals elongate into ellipsoids and then recover their original shape after unloading. The plasmon peak intensity showed an irreversible decrease after unloading. The reduced absorbance peak intensity after unloading is correlated to the formation of defects in nanocrystals through a damping factor [2]. The optical data supports the conclusion that the irreversible increase in XRD peak width after pressure cycling is due to the formation of crystalline defects, rather than a change in the size and shape of crystalline domains within the nanocrystals. UV-vis absorbance provides conclusive information about nanocrystal shape, and XRD provides conclusive information about defect formation.

MD simulations were used to understand the crystalline defects that form within the nanocrystals, and their interactions with existing twin boundaries and surfaces. Two types of

stacking faults (SF) were formed in an icosahedral nanocrystal under pressure (Fig. 3A); SF type 1 refers to a stacking fault parallel to the outer surface of the nanocrystal (or parallel to surface steps formed during deformation), and SF type 2 is a stacking fault parallel to an internal twin boundary that intersects with two other twin boundaries. Both types of stacking fault were formed by the nucleation and propagation of a Shockley partial dislocation with a Burgers vector of $\frac{1}{6}\langle 112\rangle a$. SF type 1 forms when a Shockley partial dislocation with Burgers vector parallel to the outer surface propagates on a slip plane parallel to the outer surface. This results in a displacement relative to adjacent grains that is about the magnitude of the Burgers vector (see the Supplementary Material [14]). When trailing partials are activated on the same plane, the stacking fault is removed, which results in the formation of a larger displacement. The trailing partial slip in one grain sometimes triggers stacking fault formation in an adjacent grain. This occurs if the Burgers vector of the trailing partial dislocation (i.e. the slip direction) is aligned well with the Burgers vector of a leading partial dislocation (Fig. 3B). SF type 2 is a dislocation that has a Burgers vector parallel to an interior twin boundary. The passage of SF type 2 is blocked by intersecting twin boundaries and forms interfacial dislocations with a $\frac{1}{9}\langle 222\rangle a$ Burgers vector. This type of stacking fault has also been observed in penta-twinned silver nanowire with >40 nm diameter [39]. In contrast to the penta-twinned silver nanowires, the trailing partial does not follow the leading partial (or, the SF type 2) in the 3.9 nm nanocrystal because the image stress is very large due to the proximity to the free surface and opposes the motion of the trailing partial. For this reason, SF type 2 is harder to form, and the plastic deformation of the nanocrystal is dominated by the successive formation of SF type 1 defects. This is in contrast with work by Sun et al. on Ag nanocrystals where they reported liquid like deformation via surface diffusion; however, they had performed very high temperature MD simulations to observe diffusion activity in MD time

184 scale [1]. We conducted room-temperature MD simulations where surface diffusion was limited.
185 This is in line with experiments where the Au nanocrystal surface was protected by bulky organic
186 ligands that form Au-SR bonds which prevent diffusion at the nanocrystal surface [40].

187 We attribute the irreversible deformation in the nanocrystals to SF type 1 defects, as
188 portions of these defects remain in the simulated nanocrystal after unloading (See Fig. 3B). The
189 stacking fault parallel to the outer surface is energetically meta-stable, because of the finite energy
190 barrier required to form a partial dislocation to reversely sweep out the stacking fault. In
191 experimental time scales, some meta-stable stacking faults can be expected to remain. In contrast,
192 SF type 2 escapes quickly to the free surface during unloading upon the removal of deviatoric
193 stress, which implies that the plastic deformation by this type of stacking fault is reversible. SF
194 type 2 forms a partial dislocation loop that is blocked by twin boundaries. This is an unstable
195 structure that is easily pulled towards the free surface by an image stress [39].

196 The correspondence between the experimental data and MD simulation was evaluated by
197 generating XRD patterns from the MD simulated structures at different pressures by using the
198 Debye scattering equation [24] (see Fig. 4A-B). The Debye scattering equation is a Fourier
199 transform of the interatomic distances in a nanocrystal. Large ripples are observed in the computed
200 patterns due to the small number of atoms in a finite sized nanocrystal (see Fig. S10). These ripples
201 become less prominent when diffraction patterns for different sized nanocrystals are combined.
202 Figure 4 shows the average XRD pattern for 3.5, 3.9, and 4.5 nm icosahedral and 4 nm decahedral
203 nanocrystals to mimic the experimental nanocrystal size distribution. A small ripple to the left of
204 (111), and to the right of (200) and (220) can still be observed in Figure 4. While these ripples
205 could be further smoothened by simulating the same nanocrystal size distribution as in
206 experiments, this is infeasible due to constraints on computing time. The XRD peaks were fitted

using Lorentzian and Gaussian peak profile with a high order polynomial for the background. Due to the ripple on the (220) peak, the exact (220) peak width cannot be obtained but can still be analyzed qualitatively. The XRD peak width for the simulated patterns showed a similar trend to experimental data in that the (111) peak width broadened the least, and the (200) peak broadened the most under pressure (Fig. 4C-D). The (220) peak width also increased, similarly to experiments (Fig. S11). The effect of adding stacking faults to the nanocrystal is evident from the significant increase of peak width for the (200) and (220) peaks. The close agreement of MD simulated XRD patterns and experimental XRD patterns shows that MD simulations are a true representation of experiments.

In summary, using high-pressure XRD, optical absorbance spectroscopy and MD simulations we provide the first evidence of plastic deformation in individual 3.9 nm Au nanocrystals. The plastic deformation governed was by stacking faults formed via surface nucleated partial dislocations. The formation of surface steps during the passage of sequential partial dislocations as well as remaining stacking faults led to residual defects in the nanocrystal. The kinetics of residual defect recovery after unloading the sample will be explored further in future studies. This work provides a critical advancement in using experimental and simulation generated XRD as a comprehensive measurement technique to study defect formation in nanomaterials.

References

[1] J. Sun, L. He, Y.-C. Lo, T. Xu, H. Bi, L. Sun, Z. Zhang, S. X. Mao, and J. Li, Nat. Mater. **13**, 1007 (2014).

[2] X. W. Gu, L. A. Hanson, C. N. Eisler, M. A. Koc, and A. P. Alivisatos, Phys. Rev. Lett. **121**, 056102 (2018).

[3] A. Sharma, N. Gazit, L. Klinger, and E. Rabkin, Adv. Funct. Mater. 1807554 (2019).

[4] H. Zheng, A. Cao, C. R. Weinberger, J. Y. Huang, K. Du, J. Wang, Y. Ma, Y. Xia, and S. X. Mao, Nat. Commun. **1**, 144 (2010).

[5] P. Liu, L. Wang, Y. Yue, S. Song, X. Wang, K. M. Reddy, X. Liao, Z. Zhang, M. Chen, and X. Han, Nanoscale **11**, 8727 (2019).

[6] Y. Lu, J. Song, J. Y. Huang, and J. Lou, Nano Res. **4**, 1261 (2011).

[7] J. Wei Wang, S. Narayanan, J. Yu Huang, Z. Zhang, T. Zhu, and S. X. Mao, Nat. Commun. **4**, 2340 (2013).

[8] L. Zhong, F. Sansoz, Y. He, C. Wang, Z. Zhang, and S. X. Mao, Nat. Mater. **16**, 439 (2017).

[9] S. Sun, D. Kong, D. Li, X. Liao, D. Liu, S. Mao, Z. Zhang, L. Wang, and X. Han, ACS Nano **13**, 8708 (2019).

[10] D. Guo, G. Xie, and J. Luo, J. Phys. D. Appl. Phys. **47**, 013001 (2014).

[11] Z. Budrovic, H. Van Swygenhoven, P. M. D. S. Van Petegem, and B. Schmitt, Science (80-.). **304**, 273 (2004).

[12] B. Chen, K. Lutker, S. V. Raju, J. Yan, W. Kanitpanyacharoen, J. Lei, S. Yang, H. R. Wenk, H. K. Mao, and Q. Williams, Science (80-.). **338**, 1448 (2012).

[13] S. Peng, Y. Lee, C. Wang, H. Yin, S. Dai, and S. Sun, Nano Res. **1**, 229 (2008).

[14] See Supplemental Material at [URL will be inserted by publisher], which includes Refs. [2, 13, 15-29] for materials and methods, calculations, additional XRD and optical absorbance spectroscopy.

[15] C. Herbst, R. . Cook, and H. . King, J. Non. Cryst. Solids **172**–**174**, 265 (1994).

[16] H. K. Mao, J. Xu, and P. M. Bell, J. Geophys. Res. **91**, 4673 (1986).

[17] C. Prescher and V. B. Prakapenka, High Press. Res. **35**, 223 (2015).

[18] S. Plimpton, J. Comput. Phys. **117**, 1 (1995).

[19] H. W. Sheng, M. J. Kramer, A. Cadien, T. Fujita, and M. W. Chen, Phys. Rev. B **83**, 134118 (2011).

[20] W. G. Hoover and B. L. Holian, Phys. Lett. A **211**, 253 (1996).

[21] A. Stukowski, Model. Simul. Mater. Sci. Eng. **18**, 015012 (2010).

[22] A. Cervellino, C. Giannini, and A. Guagliardi, J. Appl. Crystallogr. **36**, 1148 (2003).

[23] I. Kantor, V. Prakapenka, A. Kantor, P. Dera, A. Kurnosov, S. Sinogeikin, N. Dubrovinskaia, and L. Dubrovinsky, Rev. Sci. Instrum. **83**, 125102 (2012).

[24] A. Cervellino, R. Frison, F. Bertolotti, and A. Guagliardi, J. Appl. Crystallogr. **48**, 2026 (2015).

[25] A. Dewaele, P. Loubeyre, and M. Mezouar, Phys. Rev. B **70**, 094112 (2004).

[26] X. Hong, T. S. Duffy, L. Ehm, and D. J. Weidner, J. Phys. Condens. Matter **27**, 485303 (2015).

[27] A. K. Singh, C. Balasingh, H. K. Mao, R. J. Hemley, and J. Shu, J. Appl. Phys. **83**, 7567 (1998).

[28] T. S. Duffy, G. Shen, D. L. Heinz, J. Shu, Y. Ma, H.-K. Mao, R. J. Hemley, and A. K. Singh, Phys. Rev. B **60**, 15063 (1999).

[29] A. K. Singh, H. P. Liermann, S. K. Saxena, H. K. Mao, and S. U. Devi, J. Phys. Condens. Matter **18**, S969 (2006).

[30] B. Palosz, E. Grzanka, S. Gierlotka, S. Stel´makh, R. Pielaszek, U. Bismayer, J. Neuefeind, H.-P. Weber, T. Proffen, R. Von Dreele, and W. Palosz, Zeitschrift Für Krist. - Cryst. Mater. **217**, 497 (2002).

[31] C. A. Herbst, R. L. Cook, and H. E. King Jr., J. Non. Cryst. Solids **172**–**174**, 265 (1994).

[32] B. Li, X. Wen, R. Li, Z. Wang, P. G. Clem, and H. Fan, Nat. Commun. **5**, 4179 (2014).

[33] B. Li, K. Bian, J. M. D. Lane, K. M. Salerno, G. S. Grest, T. Ao, R. Hickman, J. Wise, Z. Wang, and H. Fan, Nat. Commun. **8**, 14778 (2017).

[34] Z. Wang, C. Schliehe, T. Wang, Y. Nagaoka, Y. C. Cao, W. A. Bassett, H. Wu, H. Fan, and H. Weller, J. Am. Chem. Soc. **133**, 14484 (2011).

[35] A. K. Singh, J. Appl. Phys. **73**, 4278 (1993).

[36] B. D. Cullity and S. R. Stock, *Elements of X-Ray Diffraction* (2014).

[37] K. Takemura and A. Dewaele, Phys. Rev. B **78**, 104119 (2008).

[38] A. Vincenzo, P. Roberto, F. Marco, M. M. Onofrio, and I. Maria Antonia, J. Phys. Condens. Matter **29**, 203002 (2017).

[39] R. A. Bernal, A. Aghaei, S. Lee, S. Ryu, K. Sohn, J. Huang, W. Cai, and H. Espinosa, Nano Lett. **15**, 139 (2015).

[40] P. Ionita, A. Volkov, G. Jeschke, and V. Chechik, Anal. Chem. **80**, 95 (2008).

Acknowledgements:

We thank Zhongwu Wang at Cornell High Energy Synchrotron Source for supporting this project. X.W.G. and A.P. acknowledge financial support from Stanford start-up funds. The Advanced Light Source is supported by the Director, Office of Science, Office of Basic Energy Sciences, of the U.S. Department of Energy under Contract No. DE-AC02-05CH11231. Beamline 12.2.2 is partially supported by COMPRES, the Consortium for Materials Properties Research in Earth Sciences under NSF Cooperative Agreement EAR 1606856. Part of this work was performed at the Stanford Nano Shared Facilities (SNSF), supported by the National Science Foundation under award ECCS-1542152. M.T.K. is supported by the National Defense and Science Engineering Graduate Fellowship. D.D. is supported by the NSF Graduate Fellowship. S.L. and S.R. are supported by the Creative Materials Discovery Program (2016M3D1A1900038) through the National Research Foundation of Korea (NRF) funded by the Ministry of Science and ICT. L.A.H. and K.A.H. acknowledge financial support from Trinity College.

Figures

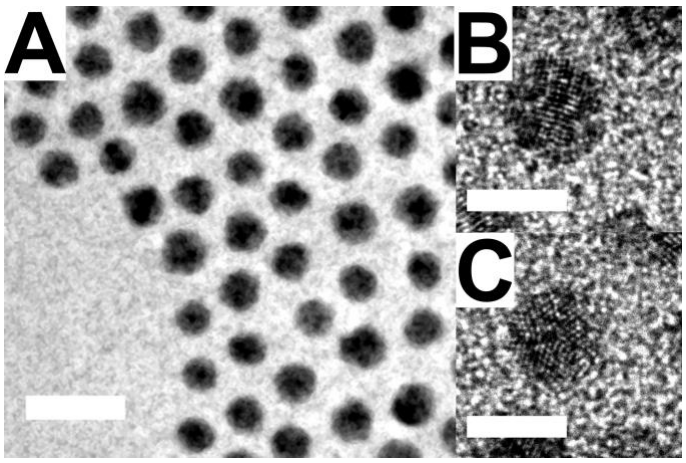

Fig. 1. TEM images of nanocrystals. A) Monodisperse 3.9 nm Au nanocrystals. Scale bar is 10 nm. High-resolution images of B) icosahedral and C) decahedral nanocrystals. Scale bar is 4 nm.

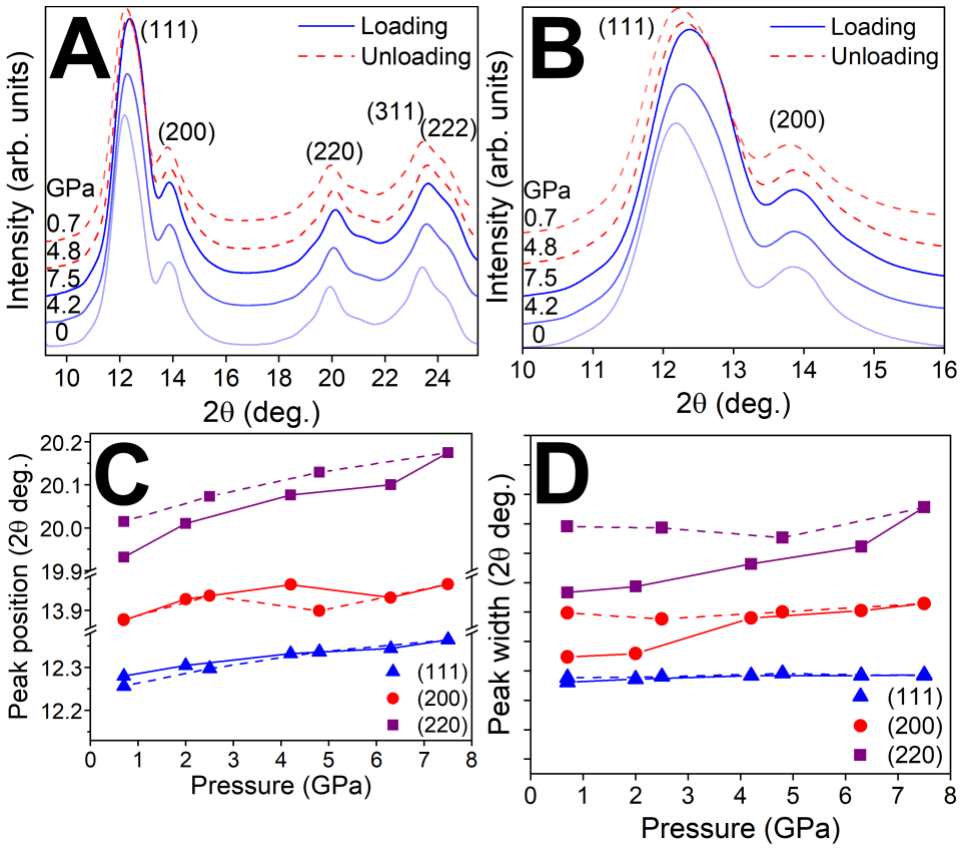

310

311 **Fig. 2. Experimental high-pressure XRD patterns.** A) All diffraction peaks and B) magnified

312 view of (111) and (200) peaks. Change in diffraction peak C) position and D) width (each

313 division is 0.1º), upon loading (solid line) and unloading (dashed line).

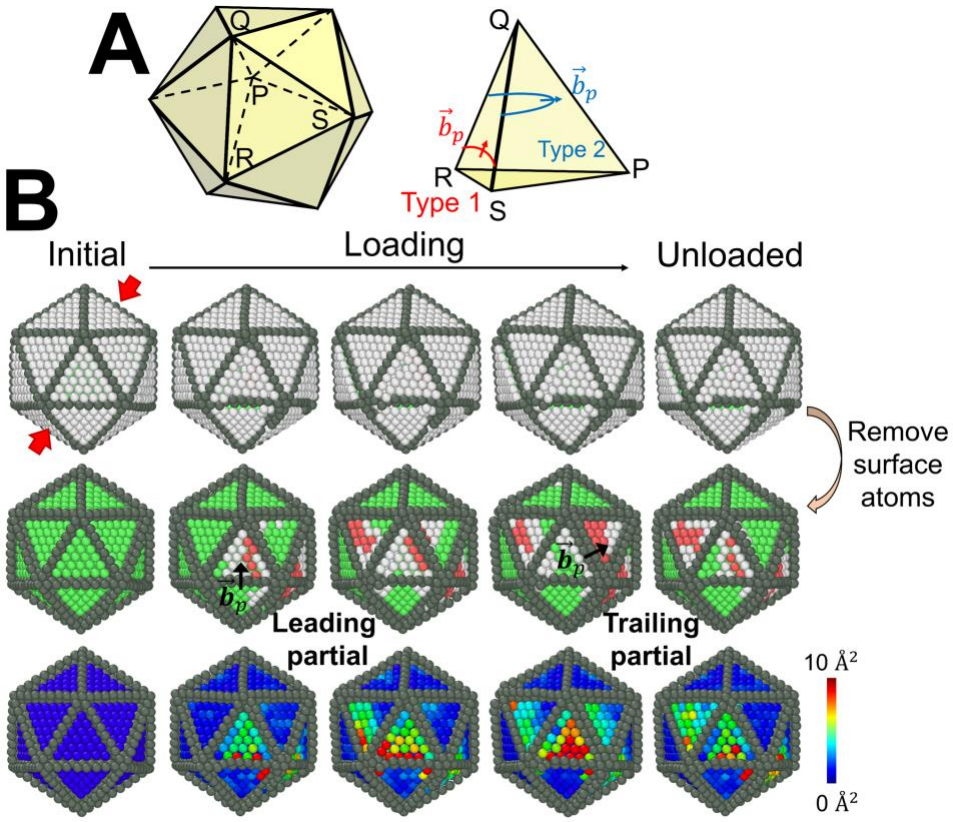

Fig. 3. MD simulation of a 3.9 nm icosahedral nanocrystal. A) Schematic of nanocrystal geometry and slip planes for stacking fault type 1 and type 2. B) Atomic configurations during loading and unloading process. Top row shows the surface atoms and the loading direction (red arrows). In the next two rows, outermost atoms are omitted to visualize the formation of defects. Images in middle row have green atoms for FCC, white atoms for unclassified crystal structure (typically near the core of a partial dislocation or at the surface), and red atoms for HCP. Images in bottom row are colored according to non-affine squared displacement, in which the slip plane swept by a perfect dislocation is identified.

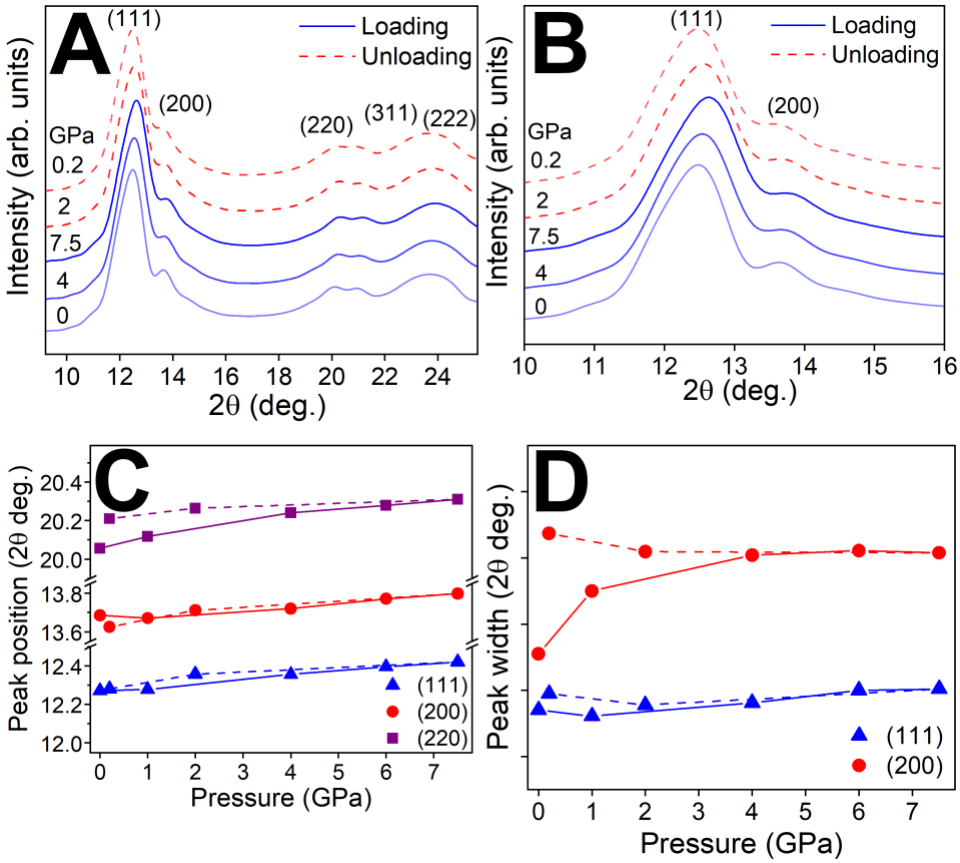

Fig. 4. Simulated high-pressure XRD patterns from MD simulations. A) All diffraction peaks and B) magnified view of (111) and (200) peaks. Change in diffraction peak C) position and D) width (each division is 0.1°), upon loading (solid line) and unloading (dashed line).